### **Article**



# Insights into substrate transport and water permeation in the mycobacterial transporter MmpL3

Yupeng Li, <sup>1,2</sup> Atanu Acharya, <sup>3</sup> Lixinhao Yang, <sup>4</sup> Jinchan Liu, <sup>5</sup> Emad Tajkhorshid, <sup>1,2,6</sup> Helen I. Zgurskaya, <sup>7</sup> Mary Jackson, <sup>8</sup> and James C. Gumbart <sup>3,4,\*</sup>

<sup>1</sup>Theoretical and Computational Biophysics Group, NIH Resource for Macromolecular Modeling and Visualization, Beckman Institute for Advanced Science and Technology, University of Illinois Urbana-Champaign, Urbana, Illinois; <sup>2</sup>Center for Biophysics and Quantitative Biology, University of Illinois Urbana-Champaign, Urbana, Illinois; <sup>3</sup>School of Physics, Georgia Institute of Technology, Atlanta, Georgia; <sup>4</sup>School of Chemistry and Biochemistry, Georgia Institute of Technology, Atlanta, Georgia; <sup>5</sup>Department of Molecular Biophysics and Biochemistry (MB&B), Yale University, New Haven, Connecticut; <sup>6</sup>Department of Biochemistry, University of Illinois at Urbana-Champaign, Urbana, Illinois; <sup>7</sup>Department of Chemistry and Biochemistry, University of Oklahoma, Norman, Oklahoma; and <sup>8</sup>Mycobacteria Research Laboratories, Department of Microbiology, Immunology and Pathology, Colorado State University, Fort Collins, Colorado

ABSTRACT Mycobacteria, such as *Mycobacterium tuberculosis*, are characterized by a uniquely thick and waxy cell envelope that consists of two membranes, with a variety of mycolates comprising their outer membrane (OM). The protein Mycobacterial membrane protein Large 3 (MmpL3) is responsible for the transport of a primary OM component, trehalose monomycolate (TMM), from the inner (cytoplasmic) membrane (IM) to the periplasmic space, a process driven by the proton gradient. Although multiple structures of MmpL3 with bound substrates have been solved, the exact pathway(s) for TMM or proton transport remains elusive. Here, employing molecular dynamics simulations we investigate putative pathways for either transport species. We hypothesized that MmpL3 will cycle through similar conformational states as the related transporter AcrB, which we used as targets for modeling the conformation of MmpL3. A continuous water pathway through the transmembrane region was found in one of these states, illustrating a putative pathway for protons. Additional equilibrium simulations revealed that TMM can diffuse from the membrane into a binding pocket in MmpL3 spontaneously. We also found that acetylation of TMM, which is required for transport, makes it more stable within MmpL3's periplasmic cavity compared with the unacetylated form.

SIGNIFICANCE Mycobacteria are the causative agents of a number of infectious diseases, most notably tuberculosis. These bacteria are characterized by a thick, hydrophobic cell envelope containing primarily mycolates. The membrane-bound MmpL3 is an essential protein responsible for transporting trehalose mycolates from the inner membrane to the periplasm, although the full transport pathway has yet to be resolved. Using extensive molecular dynamics simulations, we further characterize two known substrate binding sites on the pathway and identify how the substrate may move between them. Additionally, we observe water permeation through MmpL3 only in a specific conformation, which may provide a pathway for protons that is necessary for energizing transport. Insights into MmpL3 function can inform the rational development of new anti-mycobacterial drugs.

### INTRODUCTION

Mycobacterium tuberculosis (Mtb), the causative agent of tuberculosis (TB), poses an immense threat to human health with an estimated 2 billion people around the world infected

Submitted October 17, 2022, and accepted for publication March 10, 2023. \*Correspondence: gumbart@physics.gatech.edu

Atanu Acharya's present address is BioInspired Syracuse and Department of Chemistry, Syracuse University, Syracuse, New York.

Yupeng Li and Atanu Acharya contributed equally to this work.

Editor: Philip Biggin.

https://doi.org/10.1016/j.bpj.2023.03.018

© 2023 Biophysical Society.

latently (1). Between 5% and 10% of latent infections progress to active TB cases (2), leading to approximately 1.5 million deaths per year (1). The death rate from TB is 50% without treatment. Available treatments reduce this to 15% (1) but require a combination of four drugs given for 4–6 months (3,4). However, even this treatment protocol is facing great challenges due to the emergence of drug-resistant Mtb (5). Equipped by its thick and waxy cell envelope, which is composed of glycans and two membranes (6), Mtb is extraordinarily resistant to drugs and antibiotics, calling for novel antibacterial approaches to treat its infections (7).



One of the most distinct components accounting for the unusually thick cell envelope in Mtb are mycolic acids, fatty acids present in the bacterium's outer membrane (OM) with lipid tails 60–90 carbon atoms long (8,9). Multiple types of mycolic acids are found in Mtb, such as trehalose dimycolates (TDMs) (8), the cord factor actively involved in TB pathogenesis (10,11). During the biogenesis of TDM its precursor, trehalose monomycolate (TMM), is transported across the inner membrane (IM) by the essential protein Mycobacterial membrane protein Large 3 (MmpL3) (12,13). The enzyme complex called Ag85 then catalyzes TMM maturation into TDM (14). Because of its key role, MmpL3 is an attractive target for developing drugs against TB (15-17); by inhibiting MmpL3-mediated transport, TMM would be unavailable for TDM biogenesis (18,19). The strategy has been validated by the development of a series of new potential antibiotics (17), AU1235 (19), BM212 (16), and SQ109 (15), the last of which has completed phase 2b-3 clinical trials (20). With the early success so far in targeting MmpL3, an improved understanding of the molecular mechanisms of MmpL3-mediated transport can assist in the further development of much needed novel antibiotics against TB.

MmpL3 belongs to the resistance-nodulation-division (RND) superfamily of transporters that actively transports substrates such as proteins, lipids, and other small molecules by using the proton gradient across the IM (21,22). The first high-resolution structure of MmpL3 was solved in 2019 (23), revealing two periplasmic subdomains and 12 transmembrane helices (TMs 1-12; see Fig. 1) (23). TM4 and TM10 come together to form two Asp-Tyr dyads presumably involved in the proton transfer, as suggested by mutagenesis experiments (24). The two Asp-Tyr dyads form hydrogen bonds with each other, connecting TM4 and TM10. TM7 to TM10 form a hydrophobic binding pocket located in the periplasmic half of the protein, while a cavity formed between the two periplasmic domains can accommodate a TMM extracted from the membrane. Additionally, two binding sites for TMM were identified in the recent MmpL3 structure from Mycobacterium smegmatis (MmpL3smg) (25). Although the binding sites have been resolved, the exact mechanism of TMM transport by MmpL3 and how protons are coupled to the process remain unclear.

The acriflavine resistance B protein (AcrB) is also an RND transporter (26) and may have functional similarities to MmpL3. AcrB forms a trimer in the IM of Gram-negative bacteria and is part of a larger efflux pump that exports toxic substances, thus providing an innate means of antibiotic resistance (27–29). The recognition and export of toxic substances are enabled by a cycle of three distinct states of AcrB characterized by high-resolution structures (30), the loose (L), tight (T), and open (O) states (31). Specifically, recognition happens in the L state, where the toxic substance binds to an access pocket open to the periplasm. As AcrB transitions from the L state to the T state, the substrate

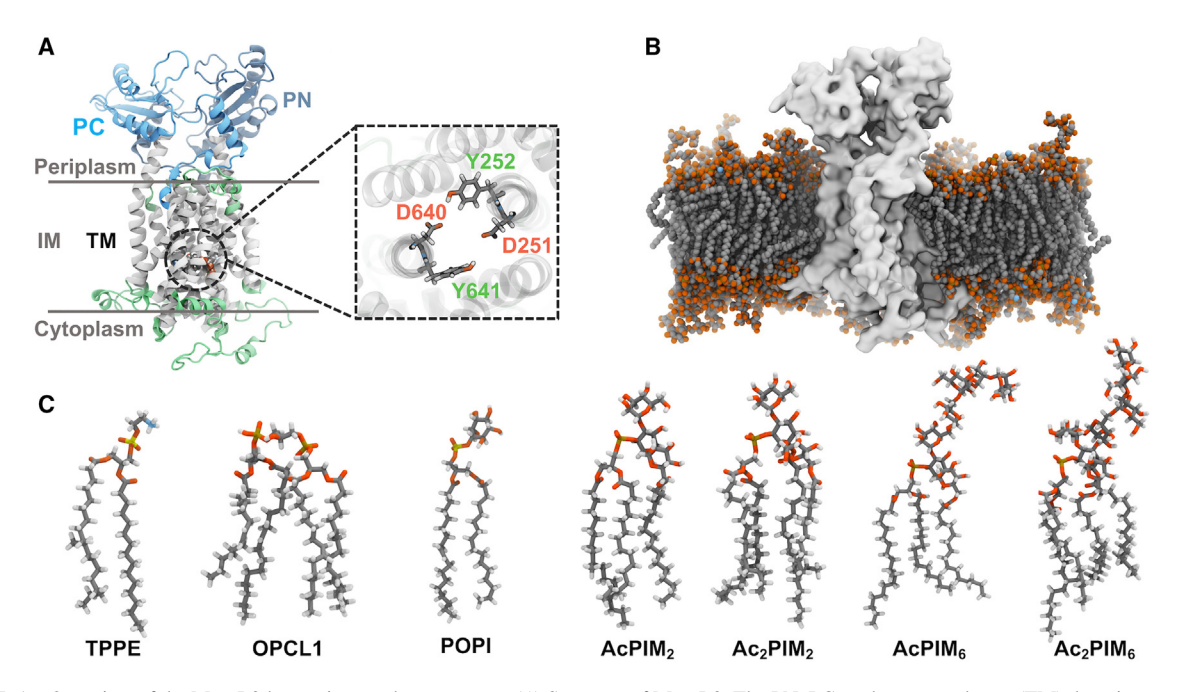


FIGURE 1 Overview of the MmpL3tb protein-membrane system. (A) Structure of MmpL3. The PN, PC, and transmembrane (TM) domains are shown in dark blue, light blue, and white, respectively, while the remaining regions of the protein are shown in green. Key hydrogen-bonding residues in the TM domain are highlighted in the inset, which shows the central hydrogen-bonding dyads D251 - Y252 ··· D640 - Y641 in the periplasmic side of MmpL3. (B) MmpL3 embedded in the mycobacterial IM. MmpL3 is shown in a surface representation while lipids are shown by spheres, in which carbon, oxygen, nitrogen, and phosphorus atoms are in gray, red, blue, and tan, respectively. (C) Structures of individual mycobacterial IM lipids. Lipids are colored in the same way as in (B), with the addition of hydrogens in white. To see this figure in color, go online.

is translocated into a deep binding pocket. During the transition from the T state to the O state, the deep binding pocket opens up to the lumen of the attached periplasmic AcrA and OM channel TolC, which permits the expulsion of the substrate to the extracellular space.

With inspiration from AcrB, we hypothesized that MmpL3 will follow a similar cycle and used the L, T, and O states of AcrB to generate corresponding states for MmpL3. These L/T/O-like states were then relaxed with molecular dynamics (MD) simulations during which water was found to penetrate the transmembrane domain. Moreover, we simulated TMM at different binding sites in MmpL3 to determine its behavior and interactions with the protein. Since the acetylation of TMM was reported to be necessary for the transport (32,33), both the acetylated (AcTMM) and the deacetylated forms of TMM were simulated to study how acetylation affects binding. We also used targeted molecular dynamics (TMD) to drive TMM from the binding pocket to the periplasmic cavity, thereby mapping out a potential transport pathway for it.

#### MATERIALS AND METHODS

### System preparation

MmpL3tb 1-752 was constructed from a recent cryo-electron microscopy (cryo-EM) structure (PDB: 7NVH) (34). The missing residues (343–377) were built by SWISS-MODEL (35); for comparison, we also show the AlphaFold 2 (36) model for this segment in Fig. S1. We then embedded the resulting MmpL3 into a native mycobacterial IM using the membrane builder module of CHARMM-GUI (37,38). Since mycobacterial phospholipids are not currently available in CHARMM-GUI, lipids with structures similar to phosphatidylinositol mannosides (PIMs) and others were built initially and modified later. This premodified membrane consisted of multiple types of phospholipids, including 1,2-distearoyl-sn-glycero-3phosphorylethanolamine (DSPE), tetraoleoyl cardiolipin (TOCL1), 1-palmitoyl-2-oleoyl-sn-glycero-3-phosphatidylinositol (POPI), and four groups of glycolipids for construction of PIMs (39). The sugar sequence of glycolipids is shown in Fig. S1. The resulting protein-membrane system was solvated in a water box with 0.15 M KCl.

Phospholipids in the resulting protein-membrane system were further modified to mycobacterial phospholipids using VMD (40), including the tail saturation, the branched carbons on tails, the linkages of the sugars, and the acylation. The structures of mycobacterial phospholipids were taken from a previous study by Goren (39). DSPE (18:0/18:0) was modified to 1-tuberculostearoyl-2-palmitoyl-sn-glycero-3-phosphorylethanolamine (TPPE, 19 Br/16:0); TOCL1 (18:1/18:1, 18:1/18:1) was modified to 1',3'-bis[1oleoyl-2-palmitoleoyl-sn-glycero-3-phospho]-glycerol (OPCL1, 18:1/16:1, 18:1/16:1); the phosphatidylinositol (PI) tails in glycolipids were modified from 18:0/18:0 to 19 Br/16:0; POPI was not manipulated further. For PIMs, the inositol ring adopted a chair conformation with five hydroxyl groups in equatorial positions at C1, C3, C4, C5, and C6, respectively, while the last OH group was positioned axially at C2. Depending on the species, two or six  $\alpha$ -D-mannose molecules were added to the PI core of PIMs. The first mannose was added to the inositol ring by a  $2 \leftarrow 1$  linkage, and a glycosidic bond was created between the C6 of inositol ring and the C1 of sugar for the second mannose. For mannoses 2-4, the hydroxyl group on C1 was linked to C6 of the previous mannose, while C1 of mannoses 5 and 6 was attached to C2 of the last sugar. Two sites on PIM can potentially be acylated to form acylated phosphatidylinositol dimannoside (AcPIM), in which the first acyl tail (palmitoyl) is connected to C6 of the first mannose, while the second one is connected to C3 of the inositol ring of PI. The composition of the resulting mycobacterial IM is TPPE/OPCL1/POPI/AcPIM<sub>2</sub>/Ac<sub>2</sub>  $PIM_2/AcPIM_6/Ac_2 PIM_6 = 27:38:2:11:11:5.5:5.5$ . The degree of differences in the per-leaflet composition of the IM remains under debate (9). Therefore, we modeled it as a symmetric bilayer, although we note that another recent model was constructed with an asymmetric composition (41).

TMM and AcTMM were also built using VMD (40). The acetyl group of AcTMM was linked to the hydroxyl group on the mycolic tails. Since the structure of mycolates varies, we built the  $\alpha$  form of the main component of mycolates in M. tuberculosis (42,43). The corresponding mycolic acids forming TMM can be represented as CH<sub>3</sub>-(CH<sub>2</sub>)<sub>1</sub>-cyclopropyl-(CH<sub>2</sub>)<sub>m</sub>-cyclopropyl-(CH<sub>2</sub>)<sub>n</sub>-CH(OH)-CH(COOH)-(CH<sub>2</sub>)<sub>p</sub>-CH<sub>3</sub>. Here, we used 19, 14, 13, and 23 for l, m, n, and p, respectively (42,43). Both cyclopropyl groups were modeled in the cis conformation. The longer and shorter tails are denoted as merochain and  $\alpha$  branch, respectively. To obtain the AcTMM/TMM-bound MmpL3tb at the binding pocket and at the periplasmic cavity, we used the cryo-EM structure of TMM-bound MmpL3smg (PDB: 7N6B) as a template for the TMM only (25). AcTMM/TMM was first aligned with the existing TMM in MmpL3smg, and the coordinates of each atom were then set to match those in the template. The numbers of each lipid in the bilayer as well as the total number of atoms for all simulations are given in Table S1.

### **MD** simulation

MD simulations were performed by NAMD (44,45) with the CHARMM36m (46) and CHARMM36 (47) force fields for protein and lipids, respectively. Equilibration, Gaussian accelerated molecular dynamics (GaMD), and TMD simulations used NAMD 2.14 for GPUs, while all others used the GPU-resident NAMD 3.0. The TIP3P water model was used (48). The temperature was maintained at 310 K by a Langevin thermostat, while the pressure was kept at 1 atm by a Langevin piston barostat (49,50). The "flexible cell" option was enabled to allow the three dimensions of the system to change independently, while the x/y ratio of the membrane dimensions was held fixed. A 12-A cutoff was used for non-bonded interactions with a switching function starting at 10 Å. The Particle-mesh Ewald method (51) was utilized for calculating long-range electrostatic interactions at every time step. Bonds involving hydrogen atoms were kept rigid by the SHAKE (52) and SETTLE (53) algorithms. Hydrogen mass repartitioning was employed to accelerate simulations, allowing for a time step of 4 fs (54,55).

To equilibrate the membrane-protein system, a 2000-step minimization was run, followed by equilibrium simulations using successively relaxed constraints (56). First, only phospholipid tails were free to move for 1 ns, followed by releasing everything except protein for 10 ns and everything except the backbone of the protein for 10 ns; finally, everything was released for 100 ns. TMM or AcTMM was then added to the relaxed membrane-protein system in the appropriate location, either replacing a lipid in the binding pocket or being added to the periplasmic cavity. The resulting systems were minimized for 2000 steps and used for production simulations.

To find a potential transport pathway for TMM between the membranebinding pocket and the periplasmic cavity, we used TMD. The starting structure of TMM was obtained from the simulations of the system with TMM bound at the binding pocket after 25 ns, while the targeted conformation was exactly the same configuration of the system with TMM bound in the periplasmic cavity that we constructed based on the cryo-EM structure (25). The headgroup was targeted first for 50 ns, after which two carbons of the shorter tail and three carbons of the longer tail were targeted in successive 10-ns steps until the entire TMM was transported.

### **Analysis**

Since mycobacterial lipids are rarely simulated, we monitored the box dimensions (Fig. S3) as well as the area per lipid (ApL) of each type of lipid (Fig. S4) over time for each system. ApL was determined using LOOS (57,58). We also measured the helical content (the number of helical residues) over time (Fig. S5) and the fraction of time each residue was in a helical form (Fig. S6), demonstrating the stability of each system and structural similarities or differences between them.

### **RESULTS AND DISCUSSION**

### Water transport through the TM region

MmpL3-mediated transport of TMMs across the IM is poorly understood, especially how transport is coupled to the proton motive force across the membrane. The pair of hydrogen-bonded Asp-Tyr dyads, located in the TM region, was previously identified to be necessary for MmpL3 function (13,23). It has been proposed that the arrival of a proton can induce the formation of water chains across the membrane even through a greasy lipid layer (59,60). Nevertheless, the presence of a few polar residues in the TM region may be required to form a transient water wire, as proposed by Kratochvil et al. in a recent synthetic system (59). Because we are running classical MD simulations, in which mobile protons are not modeled, we have investigated the feasibility for formation of connected hydration patterns through the membrane region of MmpL3tb as a proxy for potential proton transport.

## Water permeation into MmpL3 observed during equilibrium and accelerated MD

We performed two independent equilibrium MD simulations (674 ns and 664 ns, respectively) to investigate water dynamics in MmpL3. We also determined the overall extent of water penetration into MmpL3 by calculating the water volume map within 3.5 Å of MmpL3 using the VolMap plugin of VMD (40); each map represents water accessibility in the system and is averaged over the trajectory (Fig. S7). Both Asp residues in the central Asp-Tyr dyads were modeled in their default (deprotonated) form, producing the most stable hydrogen-bonding network. While water molecules enter the TM region from the cytoplasmic side, they do not penetrate farther than the hydrogen-bonded dyads (Fig. 1 A). The stable presence of water within a membrane protein near polar residues has been observed before (59) as well as more specifically in other membrane transporters (61). Furthermore, the gating of water conduction by non-polar residues has been postulated previously in AcrB (62).

To explore the possibility of larger fluctuations creating deeper water penetration, we carried out GaMD simulations (63,64) using a 10 kcal/mol boost potential. However, even with this enhanced sampling strategy, we did not observe water density beyond the position of the central hydrogenbonded dyads. Similar water density profiles were found for both the equilibrium and GaMD simulations (Fig. S7), suggesting that the formation of a stable hydrated pathway

through MmpL3 in its experimentally solved conformation is unlikely.

### Modeling LTO-like states in MmpL3

It has been proposed that TMM transport requires changes in MmpL3's conformation (25), which must also be coupled to proton transport across the TM region. While resolving the nature of this coupling is beyond the scope of this study, we explored the possibility of MmpL3 cycling through different states that may allow water, and thus also proton, transport through the TM region. In this context, we explored three potential conformations of MmpL3, analogous to those reported for AcrB. AcrB is a trimer, and in one structure each monomer is captured in a functionally distinct L, T, or O state (PDB: 4DX7) (65). We aligned the equilibrated structure of MmpL3 to each of these states, using residues from TM helices (Fig. S8 A and Table S2), which share 42% sequence similarity. The alignment between TM helices was determined using the structural alignment tool STAMP, part of MultiSeq in VMD (40,66,67), and plotted using ESPript (68) (see Fig. S9). Three independent, 30-ns TMD simulations were then used to drive the conformation of MmpL3 to each of the corresponding L, T, and O states. We then carried out 200-ns restrained simulations for each state in which non-moving restraints were applied to the same atoms as in the TMD simulations. Additional restraints were applied to maintain the secondary structure. Finally, we ran 400-ns unrestrained equilibrium simulations of each state. We calculated the root-mean-square deviation (RMSD) of the TM region over both the restrained and unrestrained simulations, which is similar among all three states (Fig. S8 C). Root-mean-square fluctuations also appear broadly similar among all three states (Fig. S8 B), with the exception of disordered residues 343-377, which were modeled in. We also measured the number of residues in a helix over time (Fig. S5), finding them to be broadly similar, with the only small differences coming from cytoplasmic/periplasmic regions (Fig. S6).

Analyzing the water density maps from the TMD simulations, we find that water permeation through the TM region is still blocked at the hydrogen-bonded Asp-Tyr dyads (Fig. S10). However, the water density maps from subsequent restrained (Fig. 2 A) and unrestrained (Fig. 2 B) simulations clearly capture water permeation through the TM region of MmpL3. More specifically, the three conformations of MmpL3 each offer a distinct degree of access by water to the interior of the TM region, providing a possible pathway for proton transport. The T-like state (Fig. 2 B) has a continuous water pathway connecting the cytoplasmic and periplasmic sides of MmpL3. The L-like and O-like states show a similar but lower extent of water permeation through the TM region. Interestingly, the two Asp-Tyr dyads are closest in the T-like state and still form hydrogen bonds occasionally, while in the O-like and L-like states they do

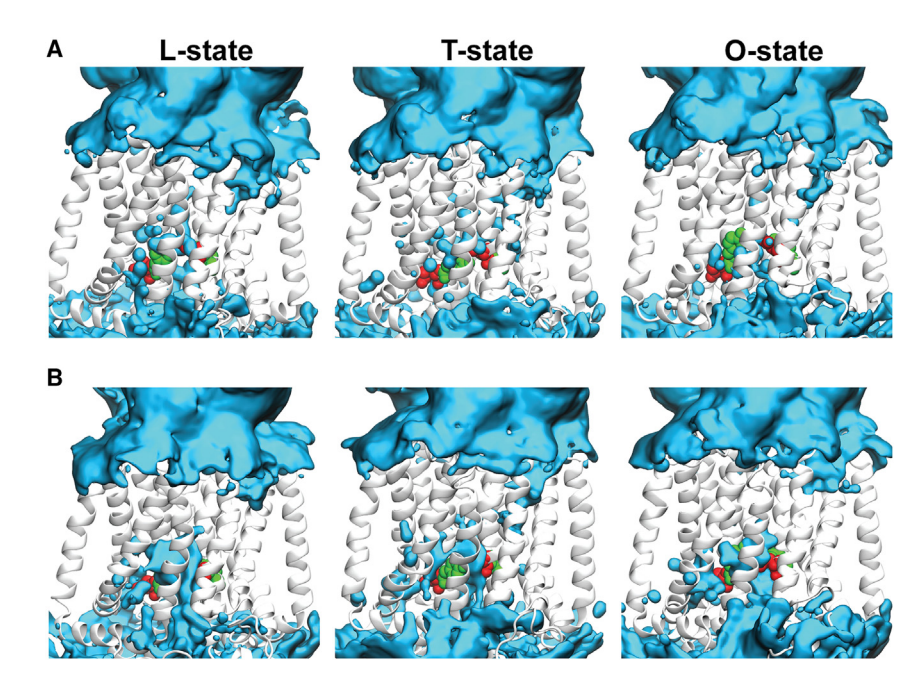


FIGURE 2 Water volume and contact maps in the TM region. Water volume maps are calculated using (A) 200-ns restrained simulations starting from the end of the TMD simulations or (B) 400-ns unrestrained simulations starting from the end of those in (A). Water density is calculated as an average over the simulation trajectories of each state using the VolMap plugin in VMD (40). Red and green spheres are Asp and Tyr residues of the dyads, respectively. To see this figure in color, go online.

not (Fig. S11). Overall, the difference in degrees of water penetration in the three states provides a potential mechanism for coupling proton transfer to substrate transport in MmpL3 in a manner analogous to AcrB.

We also analyzed the average number of water contacts to MmpL3 residues. We find that average water contacts > 5 usually happen for water-exposed domains either in the periplasm or in the cytoplasm. In contrast, residues in the TM region exhibit fewer water contacts. To represent stable and persistent water contact within the TM region, we highlight TM residues with average water contacts between 1 and 5 in Fig. S12. Again, a connected water permeation pathway is most evident in the unrestrained simulations of the T-like state. In contrast, the L-like and O-like states allow water permeation to a certain extent. These two states do not allow fully connected hydration between cytoplasm and periplasm through the TM region, as observed from the unrestrained simulations in Fig. S12.

Next, we investigated how the L-like, T-like, and O-like states differ from the initial MmpL3 structure as well as from the structure at the end of a 664-ns MD simulation (MD run #2). Both structures were used as references, and two separate RMSD calculations were performed for each state using the TM helices for alignment. The lowest average RMSD values are obtained for the TM region, while the periplasmic PN and PC domains exhibit higher average RMSD values (Table S3). For the L-like and T-like states, the PC domain has the highest average RMSD compared with either reference. In contrast, the PN domain of the T-like state has the highest average RMSD. Furthermore, the TM region is similar among the three states, as indicated by cross-state RMSD analysis (Table S4). However, the PN and PC domains are quite different among the states, despite the fact that only TM-domain residues were targeted to create these states. Thus, we conclude that subtle changes in the TM regions can induce significant conformational changes in the PN and PC domains, as indicated by higher values in the cross-state RMSD analysis.

Since we used the equilibrated structure prior to restrained simulations as a reference, we observed higher RMSD values even when comparing with the same state. For example, the PN and PC domains in the O-like state have high RMSD values compared with the reference structure, indicating significant structural changes in these domains during the simulation. A previous study also proposed that changes in the relative orientation of the PN and PC domains are essential for the transport of substrates (25). The changes in the PN and PC domains in different states modeled here may represent the initiation of the necessary PN and PC conformational changes.

### Transport of AcTMM/TMM from the binding pocket to the periplasmic domains

Multiple structures of MmpL3 with detergents, TMM analogs, or phospholipids bound to either the periplasmic cavity or the membrane-binding pocket have been determined, including lauryl maltose neopentyl glycol (LMNG) (34), dodecyl maltoside (DDM) (23), 6-n-dodecyl- $\alpha$ , $\alpha$ -trehalose (6DDTre) (23), and phosphatidylethanolamine (PE) (13). Recently, a cryo-EM structure of MmpL3smg in complex with TMM was resolved, in which the TMMs were captured in both the binding pocket and the periplasmic cavity, providing more details of the molecular interactions between MmpL3 and TMM (25). However, the mechanisms of transport remained elusive. On the one hand, much of the merochain tail of TMM was missing in this structure and no intermediate TMM-bound state was resolved; on the other hand, only one LMNG-bound structure has been determined for *Mtb* (34). Thus, connecting the two TMM-bound sites by mapping the potential pathway would provide significant insight into the mechanism of transport. In addition, the acetylation of TMM has been reported to be essential for its transport (32,33), yet its precise role during binding and transport is poorly understood. Here, we developed models and ran simulations of MmpL3tb with TMM or AcTMM bound in the binding pocket and in a cavity between the periplasmic domains. We then used TMD simulations to explore possible pathways for the transport of TMM.

### AcTMM/TMM diffuses spontaneously from the membrane into the binding pocket

We previously demonstrated with MD simulations that a PE phospholipid can spontaneously diffuse partially out of the outer leaflet of the membrane into the binding pocket formed between TM7 and TM10 of MmpL3smg (69). To further investigate the binding process of AcTMM/TMM at this binding pocket, we simulated three replicas of MmpL3tb with bound TMM or AcTMM each for 1.0  $\mu$ s. We then measured the distance along the membrane normal between the trehalose's esteric oxygen and the average phosphate plane over time. The results show that the analyzed oxygen can move significantly, up to  $\approx$ 7.5 Å above the phosphate plane (Fig. 3 B). For better visualiza-

tion, we plotted the probability distribution of this oxygen based on its relative *z* position (Fig. 3 *B*). In contrast to TMMs in a pure mycobacterial membrane (Fig. S13), we found for most replicas of the protein-membrane systems that the analyzed oxygen was located higher than the phosphate plane, further illustrating that AcTMM/TMM can be extracted from the membrane by MmpL3. Furthermore, we found that AcTMM/TMM forms a number of hydrogen bonds with the protein, primarily with residues L417, S418, L419, S522, E548, and H553 (Tables S5 and S6).

To investigate the binding affinity of AcTMM to the protein, the interaction energy between MmpL3 and the ligand (Fig. 3 C) was calculated by the NAMDEnergy plugin in VMD (40). The interaction energy was relatively stable for both TMM and AcTMM. Interestingly, one TMM system showed a noticeably lower (more favorable) interaction energy than the others. Close examination of the simulation revealed a unique conformation of TMM, in which its headgroup was crossing the tunnel that connects the two binding sites (membrane and periplasmic; Fig. 3 D). In particular, hydrogen bonding between TMM and E548 was observed only in this replica, suggesting that this residue may play a role in the transfer of TMM to the periplasmic cavity.

## AcTMM is more stable than TMM in the periplasmic cavity

To investigate the dynamics of AcTMM/TMM when bound to the periplasmic cavity, we constructed an

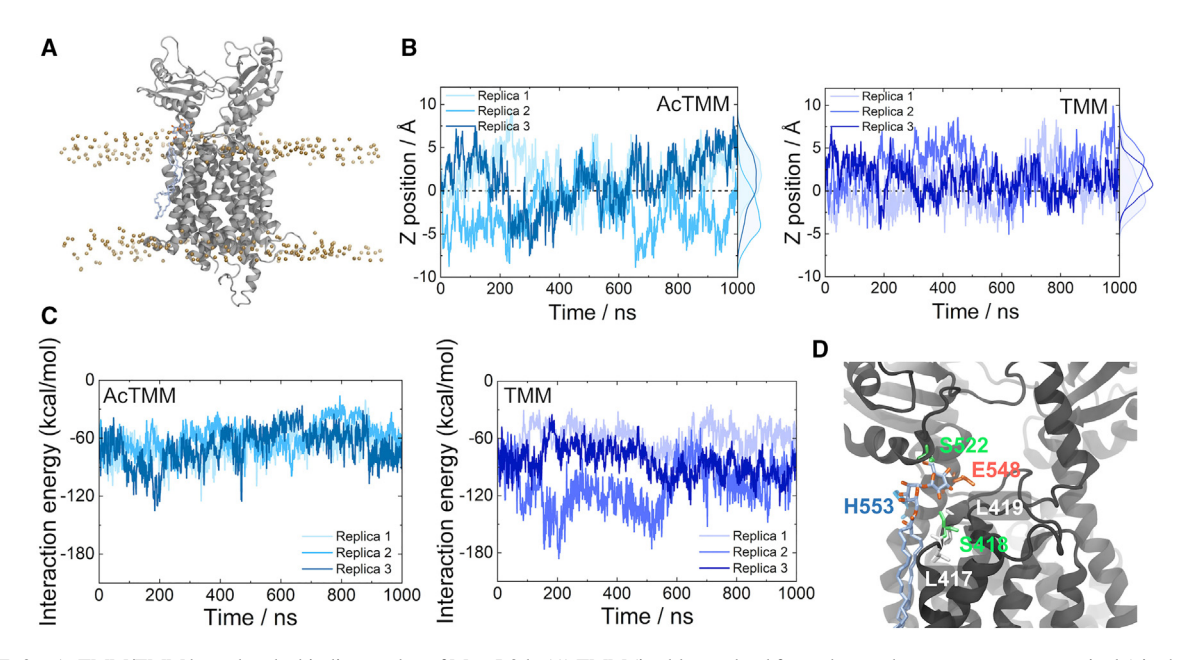


FIGURE 3 AcTMM/TMM bound to the binding pocket of MmpL3tb. (A) TMM (ice blue and red for carbon and oxygen atoms, respectively) in the binding pocket formed between TMs 7 and 10 of MmpL3tb (gray). Tan spheres represent the phosphorus atom of lipids. (B) The z position over time ( $main\ graph$ ) of the trehalose oxygen in the (left) AcTMM or (right) TMM ester group with respect to the phosphorus plane of the membrane (z=0). Probability distributions are shown on the right side of each plot. (C) The interaction energy between MmpL3 and AcTMM (left) or TMM (right). (D) TMM crossing the tunnel between the binding pocket and periplasmic cavity. The residues frequently hydrogen bonding with the TMM headgroup are highlighted, with acidic residues in red, basic in blue, polar in green, and non-polar in white. To see this figure in color, go online.

AcTMM/TMM-bound model for MmpL3tb using the cryo-EM structure of TMM-bound MmpL3smg (PDB: 7N6B) (25) as a template. After equilibration, we ran three independent simulation replicas without any restraints for 1.0 µs each. We then measured the RMSD of AcTMM/TMM in each system. Since AcTMM/TMM has exceptionally long tails, they will contribute the most to the RMSD. Therefore, to eliminate their influence, we aligned the protein first, followed by calculating the RMSD of only the headgroups of the AcTMM/TMM. The results show that TMM is less stably bound in the periplasmic cavity than AcTMM (Fig. 4 B). Two out of three replicas of the AcTMM system exhibited RMSD values of  $\approx 6$  Å while for the TMM system, the RMSD values were notably larger and more variable in all three replicas. Hydrogen bonding between the protein and AcTMM/TMM (Fig. S14), however, was similar in all the systems.

Fig. 4, C and D show two AcTMM/TMM binding poses observed in the simulations. For AcTMM, the trehalose headgroup formed hydrogen bonds with Y44, D64, N450, R448, and T544 (Table S7). The acetyl group of AcTMM was surrounded by A164, G165, I422, Q437, and F440, which potentially stabilized the whole molecule through hydrophobic effects. In contrast, TMM adopted a noticeably different conformation. The position of the entire TMM shifted down (toward the membrane), yet with the headgroup moving up (away from the membrane). Hydrogen-bonding residues for TMM were Y44, D58, D64, S66, H68, and D139 (Table S8). Therefore, we conclude that acetylation of TMM stabilizes it further in the periplasmic cavity.

### Potential transport pathway of TMM from TMD

To connect the two TMM binding sites and identify a potential transport pathway, we employed TMD to drive the TMM transport process. The initial and targeted conformations were directly derived from the above simulations (see details in materials and methods). We targeted the headgroup first, followed by TMD for the hydrophobic tails. The results show that TMM passed through the tunnel formed between the binding pocket and the periplasmic cavity (Fig. 5). With the headgroup anchored to the bottom of the periplasmic cavity, TMM flipped into the cavity, after which the hydrophobic tails moved between the PN and PC domains. These observations are similar to those in a previous TMD simulation, albeit using a shorter trehalose 6-decanoate (25). While the pathway is plausible, its validation would require more extensive free-energy calculations.

### Dynamics of TMM in the membrane

We built four membrane-only systems to investigate the dynamics of TMM in the membrane. In each system, one TMM was placed in the outer leaflet and one in the inner leaflet. The membrane composition matched the one used in other simulations (see materials and methods), and each system was simulated for 450 ns.

One of the two lipid tails in TMM is much longer than the other (70); the TMM used here had an  $\alpha$ -branch tail with 24 carbons and a longer merochain tail with 52 carbons. Thus, the conformations adopted by TMMs in the membrane were

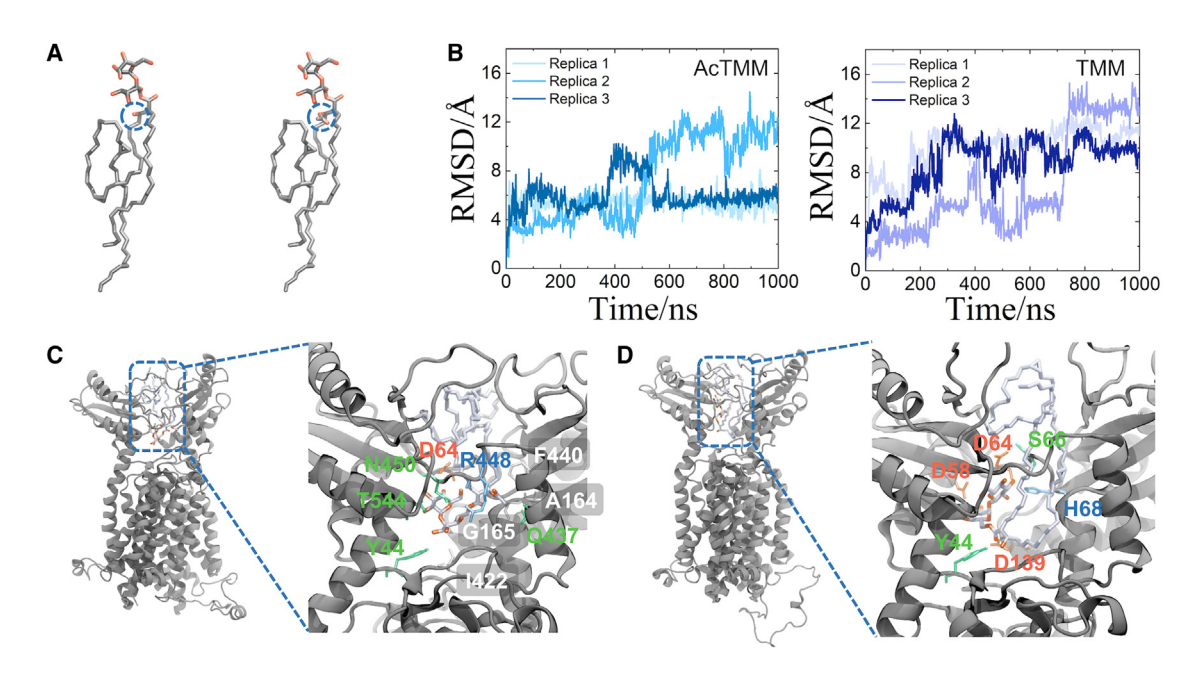


FIGURE 4 Dynamics of AcTMM/TMM bound to the periplasmic cavity of MmpL3tb. (A) Structural differences between TMM (left) and AcTMM (right). The hydroxyl group (TMM) and the acetyl group (AcTMM) are highlighted by the dashed blue circles. (B) RMSD of the trehalose headgroup for AcTMM (left) and TMM (right). (C and D) Close-up of the interactions of (C) AcTMM or (D) TMM with MmpL3. Acidic residues are colored in red, basic in blue, polar in green, and non-polar in white. To see this figure in color, go online.

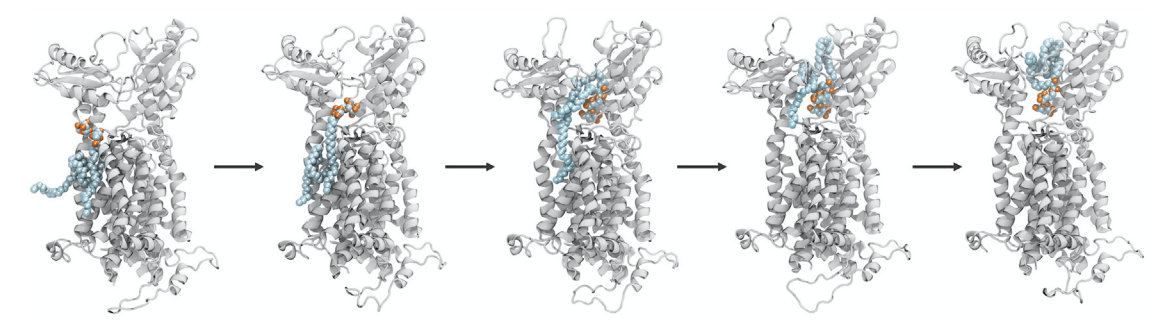


FIGURE 5 Stepwise TMD of the TMM from the binding pocket to the periplasmic cavity of MmpL3tb. TMM is shown as space-filling spheres. The headgroup of TMM was targeted first, followed by the long hydrophobic tails. To see this figure in color, go online.

more complex and varied than typical phospholipids (Fig. 1 C). Some conformations observed during the simulations are shown in Fig. 6. The shorter  $\alpha$ -branch tail usually spans just one leaflet, only occasionally sampling the other. The longer merochain tail, however, was more flexible, either occupying only one leaflet in a more compact conformation or extending into the other leaflet. Folding of the longer tail was aided by two cyclopropyl groups present at carbon atoms 14 and 30 (Fig. 7).

We also calculated the order parameters  $(S_{CH})$  of the TMM tails from the simulations according to the equation

$$S_{\rm CH} = \langle 3 \cos^2 \theta - 1 \rangle / 2,$$
 (1)

where  $\theta$  is the angle between a given CH bond and the membrane normal (Fig. 7). In general, S<sub>CH</sub> is higher for the methylene carbon atoms closer to the headgroup and lower for those near the terminus, since the latter are less ordered. While  $S_{CH}$  for the  $\alpha$ -branch tail is similar to that for phospholipids (55), the values for the merochain tail are more unusual. The first portion of the merochain tail is relatively well ordered, but there is a sharp drop in  $S_{CH}$  at the first cyclopropyl group (C14), which then persists until the next cyclopropyl group (C30). The carbon atoms between these two rings even show a slightly negative  $S_{CH}$ , indicating a large effect of the two rings on their conformation resulting in a high probability of them being oriented parallel to the bilayer surface. After the second cyclopropyl group,  $S_{\rm CH}$  rises to  $\approx 0.05$ , which may reflect conformations in which the tail traverses the other leaflet, although it is still relatively disordered. We revisited the simulations with TMM in the MmpL3 binding pocket, also finding a diversity of TMM conformations; however, there was no apparent correlation between TMM's conformations and its interaction energy with MmpL3 (Fig. S15).

We also measured the mean-squared displacement vs. time and calculated the corresponding diffusion coefficients for individual lipid types in the membrane (Table S8 and Fig. S16). Diffusion coefficients ranged from 0.61 to  $0.76 \text{ Å}^2/\text{ns}$  (6.1–7.6  $\times 10^{-8} \text{ cm}^2/\text{s}$ ). These values indicate the IM is in the fluid phase; they are also comparable with a recent study in which the mycobacterial IM was modeled (range of 0.61–1.5  $\text{Å}^2/\text{ns}$ ) (41).

### **CONCLUSIONS**

In this study, we have used MD simulations to probe possible proton and substrate transport pathways in different conformational states of the essential mycobacterial transporter MmpL3. The protein was simulated in a model mycobacterial IM. The substrate, TMM, in a pure membrane exhibits significant conformational heterogeneity, especially in its longer (52-carbon) tail. This longer tail was observed in both compact and extended conformations, sometimes crossing both leaflets (Fig. 6). Additionally, because the membrane is fluid, its rate of diffusion was found to be the same as in other lipids (Table S8).

Because of its evolutionary relationship to the transporter AcrB, we hypothesized that MmpL3 may adopt similar conformational states during its transport cycle. In particular, using structures of AcrB in L, T, and O states, we modeled analogous states of MmpL3 in the TM region. Although

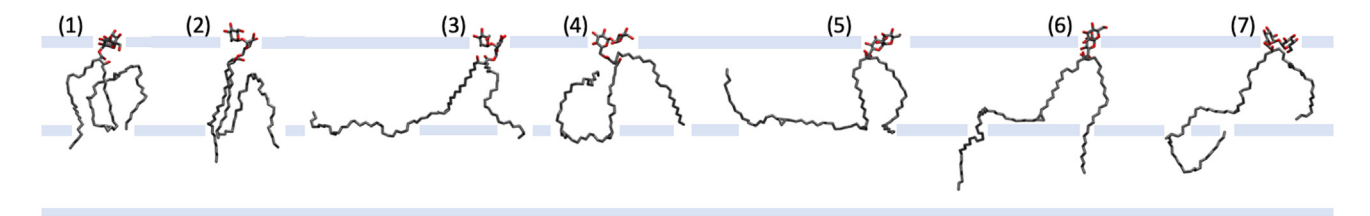


FIGURE 6 TMM conformational dynamics in the membrane. Seven selected conformations of TMM from the 4 × 450-ns simulations of pure membranes with one TMM per leaflet. To see this figure in color, go online.

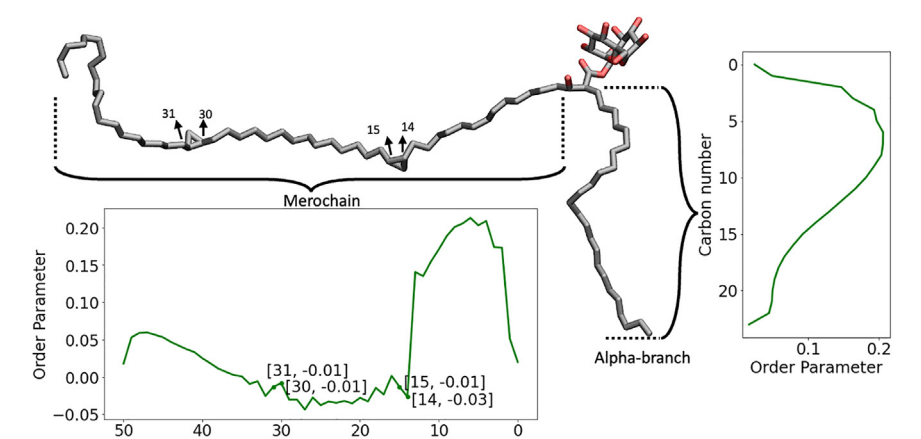


FIGURE 7 Order parameter ( $S_{\text{CH}}$ ) averaged for both TMMs over all four simulations. The plot on the right corresponds to the shorter  $\alpha$ -branch tail, while that on the left is for the longer merochain tail. One conformation of TMM is shown in the middle to indicate the tail lengths as well as the locations of the cyclopropyl rings in the merochain. To see this figure in color, go online.

the changes in the TM region were subtle, we observed larger shifts in the periplasmic PN and PC domains, demonstrating that the conformation of the TM region can influence the periplasmic domains' conformations. Additionally, a continuous pathway through the TM region was evident in an unrestrained simulation initialized in the T-like state (Fig. 2). This pathway could also be utilized by protons to reach the Asp-Tyr dyads during the transport cycle.

Carbon number

High-resolution structures of MmpL3 have revealed (so far) two binding sites for the substrate, TMM, one in a pocket exposed to the membrane (Fig. 3) and one in a cavity between the periplasmic domains (Fig. 4). Our simulations revealed spontaneous association of TMM to the membrane-binding pocket, as also reported previously (69). We also observed AcTMM to be stabilized in the periplasmic cavity relative to TMM, which may be related to the requirement of acetylation for transport of TMM (32,33). Finally, a TMD simulation provided a putative pathway between the two binding sites (Fig. 5).

Multiple aspects of MmpL3-mediated transport were investigated here, although we note that they are not all distinct. We hypothesize that substrate transport is coupled to water permeation and, thus, proton transport. MmpL3 employs a proton-substrate antiport mechanism, whereby substrate transport to the periplasm is driven by proton influx into the cytoplasm, likely utilizing water molecules for at least part of the pathway. With regard to substrate binding, we observed trapped lipids at the binding site for each proposed LTO state, regardless of the presence of a continuous water pathway, suggesting that it is independent of water permeation. Conformational dynamics of AcTMM/TMM in the membrane are also unlikely to be directly related to its binding, which primarily involves the headgroup, as previously seen for a different lipid (69).

Although our simulations have provided additional insight into possible proton and substrate pathways, the full transport cycle remains elusive. Nevertheless, the results presented here will inspire new experiments. For example,

residues along the proposed water permeation pathway can be mutated to determine whether they play a role in proton transfer. Other steps required for transport, such as TMM flipping across the IM, also remain obscure.

### **DATA AVAILABILITY**

All input files, including PSF, PDB, topology, parameter, and NAMD configuration files, along with final structures, are available at https://doi.org/10.5281/zenodo.7606596.

### SUPPORTING MATERIAL

Supporting material can be found online at https://doi.org/10.1016/j.bpj. 2023.03.018.

### **AUTHOR CONTRIBUTIONS**

Y.L., A.A., and J.C.G. designed the research with input from H.I.Z., M.J., and E.T. Y.L. and J.L. developed new models. Y.L., A.A., and L.Y. performed research and analyzed data. All authors wrote the paper.

### **ACKNOWLEDGMENTS**

This work was supported by grants from the National Institutes of Health (R01-AI116525 to M.J., H.I.Z., and J.C.G. and P41-GM104601 and R24-GM145965 to E.T.). Computational resources were provided through XSEDE (grant TG-MCB130173), which is supported by the National Science Foundation (ACI-1548562). This work also used the Hive cluster, which is supported by the NSF (MRI-1828187) and is managed by the Partnership for an Advanced Computing Environment at Georgia Tech.

### **DECLARATION OF INTERESTS**

The authors declare no competing interests.

### **REFERENCES**

WHO. 2021. Global tuberculosis report 2021. https://www.who.int/publications/i/item/9789240037021.

- Menzies, N. A., E. Wolf, ..., J. A. Salomon. 2018. Progression from latent infection to active disease in dynamic tuberculosis transmission models: a systematic review of the validity of modelling assumptions. *Lancet Infect. Dis.* 18:e228–e238.
- Nahid, P., S. E. Dorman, ..., A. Vernon. 2016. Official American thoracic society/centers for disease control and prevention/infectious diseases society of America clinical practice guidelines: treatment of drug-susceptible tuberculosis. Clin. Infect. Dis. 63:e147.
- Carr, W., E. Kurbatova, ..., C. Winston. 2022. Interim guidance: 4-month rifapentine-moxifloxacin regimen for the treatment of drugsusceptible pulmonary tuberculosis United States, 2022. MMWR Morb. Mortal. Wkly. Rep. 71:285–289.
- Cegielski, J. P., T. Dalton, ..., L. Asencios. 2014. Extensive drug resistance acquired during treatment of multidrug-resistant tuberculosis. Clin. Infect. Dis. 59:1049–1063.
- Jackson, M. 2014. The mycobacterial cell envelope-lipids. Cold Spring Harb. Perspect. Med. 4:a021105.
- Singh, R., S. P. Dwivedi, ..., T. Prasad. 2020. Recent updates on drug resistance in *Mycobacterium tuberculosis*. J. Appl. Microbiol. 128:1547–1567.
- 8. Marrakchi, H., M. A. Lanéelle, and M. Daffé. 2014. Mycolic acids: structures, biosynthesis, and beyond. *Chem. Biol.* 21:67–85.
- Jackson, M., C. M. Stevens, ..., M. Niederweis. 2021. Transporters involved in the biogenesis and functionalization of the mycobacterial cell envelope. *Chem. Rev.* 121:5124–5157.
- Hunter, R. L., M. R. Olsen, ..., J. K. Actor. 2006. Multiple roles of cord factor in the pathogenesis of primary, secondary, and cavitary tuberculosis, including a revised description of the pathology of secondary disease. Ann. Clin. Lab. Sci. 36:371–386.
- Welsh, K. J., R. L. Hunter, and J. K. Actor. 2013. Trehalose 6,6'-dimycolate – a coat to regulate tuberculosis immunopathogenesis. *Tuberculosis*. 93:S3–S9.
- Xu, Z., V. A. Meshcheryakov, ..., S.-S. Chng. 2017. MmpL3 is the flippase for mycolic acids in mycobacteria. *Proc. Natl. Acad. Sci. USA*. 114:7993–7998.
- Su, C.-C., P. A. Klenotic, ..., E. W. Yu. 2019. MmpL3 is a lipid transporter that binds trehalose monomycolate and phosphatidylethanolamine. *Proc. Natl. Acad. Sci. USA*. 116:11241–11246.
- Belisle, J. T., V. D. Vissa, ..., G. S. Besra. 1997. Role of the major antigen of *Mycobacterium tuberculosis* in cell wall biogenesis. *Science*. 276:1420–1422.
- Tahlan, K., R. Wilson, ..., H. I. Boshoff. 2012. SQ109 targets MmpL3, a membrane transporter of trehalose monomycolate involved in mycolic acid donation to the cell wall core of Mycobacterium tuberculosis. *Antimicrob. Agents Chemother*. 56:1797–1809.
- La Rosa, V., G. Poce, ..., E. De Rossi. 2012. MmpL3 is the cellular target of the antitubercular pyrrole derivative BM212. Antimicrob. Agents Chemother. 56:324–331.
- Bolla, J. R. 2020. Targeting MmpL3 for anti-tuberculosis drug development. *Biochem. Soc. Trans.* 48:1463–1472.
- Varela, C., D. Rittmann, ..., A. Bhatt. 2012. MmpL genes are associated with mycolic acid metabolism in mycobacteria and corynebacteria. Chem. Biol. 19:498–506.
- Grzegorzewicz, A. E., H. Pham, ..., M. Jackson. 2012. Inhibition of mycolic acid transport across the *Mycobacterium tuberculosis* plasma membrane. *Nat. Chem. Biol.* 8:334–341.
- Imran, M., M. K. Arora, ..., A. A. Rabaan. 2022. MmpL3 inhibition as a promising approach to develop novel therapies against tuberculosis: a spotlight on SQ109, clinical studies, and patents literature. *Biomedicines*. 10:2793.
- Tseng, T. T., K. S. Gratwick, ..., M. H. Saier. 1999. The RND permease superfamily: an ancient, ubiquitous and diverse family that includes human disease and development proteins. J. Mol. Microbiol. Biotechnol. 1:107–125.
- 22. Melly, G., and G. E. Purdy. 2019. MmpL proteins in physiology and pathogenesis of *M. tuberculosis*. *Microorganisms*. 7:70.

- 23. Zhang, B., J. Li, ..., Z. Rao. 2019. Crystal structures of membrane transporter MmpL3, an anti-TB drug target. *Cell.* 176:636–648.e13.
- 24. Bernut, A., A. Viljoen, ..., L. Kremer. 2016. Insights into the smooth-to-rough transitioning in *Mycobacterium bolletii* unravels a functional Tyr residue conserved in all mycobacterial MmpL family members. *Mol. Microbiol.* 99:866–883.
- Su, C.-C., P. A. Klenotic, ..., E. W. Yu. 2021. Structures of the myco-bacterial membrane protein MmpL3 reveal its mechanism of lipid transport. *PLoS Biol.* 19:e3001370.
- Murakami, S., and A. Yamaguchi. 2003. Multidrug-exporting secondary transporters. Curr. Opin. Struct. Biol. 13:443

  –452.
- Soto, S. M. 2013. Role of efflux pumps in the antibiotic resistance of bacteria embedded in a biofilm. *Virulence*. 4:223–229.
- Zgurskaya, H. I., V. V. Rybenkov, ..., I. V. Leus. 2018. Trans-envelope multidrug efflux pumps of Gram-negative bacteria and their synergism with the outer membrane barrier. *Res. Microbiol.* 169:351–356.
- Hazel, A. J., N. Abdali, ..., J. C. Gumbart. 2019. Conformational dynamics of AcrA govern multidrug efflux pump assembly. ACS Infect. Dis. 5:1926–1935.
- Seeger, M. A., K. Diederichs, ..., K. M. Pos. 2008. The AcrB efflux pump: conformational cycling and peristalsis lead to multidrug resistance. *Curr. Drug Targets*. 9:729–749.
- Eicher, T., M. A. Seeger, ..., K. M. Pos. 2014. Coupling of remote alternating-access transport mechanisms for protons and substrates in the multidrug efflux pump AcrB. *Elife*. 3:e03145.
- Yamaryo-Botte, Y., A. K. Rainczuk, ..., M. J. McConville. 2015. Acetylation of trehalose mycolates is required for efficient MmpL-mediated membrane transport in Corynebacterineae. ACS Chem. Biol. 10:734–746.
- Belardinelli, J. M., A. Yazidi, ..., M. Jackson. 2016. Structure–function profile of MmpL3, the essential mycolic acid transporter from *Myco-bacterium tuberculosis*. ACS Infect. Dis. 2:702–713.
- 34. Adams, O., J. C. Deme, ..., S. Newstead. 2021. Cryo-EM structure and resistance landscape of *M. tuberculosis* MmpL3: an emergent therapeutic target. *Structure*. 29:1182–1191.e4.
- Waterhouse, A., M. Bertoni, ..., T. Schwede. 2018. SWISS-MODEL: homology modelling of protein structures and complexes. *Nucleic Acids Res.* 46:W296–W303.
- Jumper, J., R. Evans, ..., D. Hassabis. 2021. Highly accurate protein structure prediction with AlphaFold. *Nature*. 596:583–589.
- Jo, S., T. Kim, V. G. Iyer, and W. Im. 2008. CHARMM-GUI: a webbased graphical user interface for CHARMM. *J. Comput. Chem.* 29:1859–1865.
- 38. Wu, E. L., X. Cheng, ..., W. Im. 2014. CHARMM-GUI membrane builder toward realistic biological membrane simulations. *J. Comput. Chem.* 35:1997–2004.
- Goren, M. B. 1984. Biosynthesis and structures of phospholipids and sulfatides. *In* The Mycobacteria, A Sourcebook, Part A Marcel Dekker, Inc., pp. 379–415.
- **40**. Humphrey, W., A. Dalke, and K. Schulten. 1996. VMD: visual molecular dynamics. *J. Mol. Graph.* 14:33–38.
- Brown, C. M., R. A. Corey, ..., M. Chavent. 2023. Supramolecular organization and dynamics of mannosylated phosphatidylinositol lipids in the mycobacterial plasma membrane. *Proc. Natl. Acad. Sci. USA*. 120:e2212755120.
- Watanabe, M., Y. Aoyagi, ..., D. E. Minnikin. 2002. Location of functional groups in mycobacterial meromycolate chains; the recognition of new structural principles in mycolic acids. *Microbiology*. 148:1881–1902.
- Minnikin, D. E., and P. J. Brennan. 2020. Lipids of clinically significant mycobacteria. *In* Health Consequences of Microbial Interactions with Hydrocarbons, Oils, and Lipids Springer, pp. 33–108.
- 44. Phillips, J. C., R. Braun, ..., K. Schulten. 2005. Scalable molecular dynamics with NAMD. *J. Comput. Chem.* 26:1781–1802.

- 45. Phillips, J. C., D. J. Hardy, ..., E. Tajkhorshid. 2020. Scalable molecular dynamics on CPU and GPU architectures with NAMD. J. Chem. Phys. 153:044130.
- 46. Huang, J., S. Rauscher, ..., A. D. MacKerell. 2017. CHARMM36m: an improved force field for folded and intrinsically disordered proteins. Nat. Methods. 14:71-73.
- 47. Klauda, J. B., R. M. Venable, ..., R. W. Pastor. 2010. Update of the CHARMM all-atom additive force field for lipids: validation on six lipid types. J. Phys. Chem. B. 114:7830-7843.
- 48. Jorgensen, W. L., J. Chandrasekhar, ..., M. L. Klein. 1983. Comparison of simple potential functions for simulating liquid water. J. Chem. Phys. 79:926-935.
- 49. Martyna, G. J., D. J. Tobias, and M. L. Klein. 1994. Constant pressure molecular dynamics algorithms. J. Chem. Phys. 101:4177–4189.
- 50. Feller, S. E., Y. Zhang, ..., B. R. Brooks. 1995. Constant pressure molecular dynamics simulation: the Langevin piston method. J. Chem. Phys. 103:4613-4621.
- 51. Darden, T., D. York, and L. Pedersen. 1993. Particle mesh Ewald: an N ·log(N) method for Ewald sums in large systems. J. Chem. Phys. 98:10089-10092.
- 52. Ryckaert, J.-P., G. Ciccotti, and H. J. Berendsen. 1977. Numerical integration of the cartesian equations of motion of a system with constraints: molecular dynamics of n-alkanes. J. Comput. Phys. 23:327-341.
- 53. Miyamoto, S., and P. A. Kollman. 1992. Settle: an analytical version of the SHAKE and RATTLE algorithm for rigid water models. J. Comput. Chem. 13:952-962.
- 54. Hopkins, C. W., S. Le Grand, ..., A. E. Roitberg. 2015. Long-time-step molecular dynamics through hydrogen mass repartitioning. J. Chem. Theory Comput. 11:1864-1874.
- 55. Balusek, C., H. Hwang, ..., J. C. Gumbart. 2019. Accelerating membrane simulations with hydrogen mass repartitioning. J. Chem. Theory Comput. 15:4673-4686.
- 56. Li, Y., J. Liu, and J. C. Gumbart. 2021. Preparing membrane proteins for simulation using CHARMM-GUI. In Structure and Function of Membrane Proteins Springer, pp. 237–251.
- 57. Romo, T. D., and A. Grossfield. 2009. LOOS: an extensible platform for the structural analysis of simulations. Annu. Int. Conf. IEEE Eng. Med. Biol. Soc. 2009:2332-2335.

- 58. Romo, T. D., N. Leioatts, and A. Grossfield. 2014. Lightweight object oriented structure analysis: tools for building tools to analyze molecular dynamics simulations. J. Comput. Chem. 35:2305-2318.
- 59. Kratochvil, H. T., L. C. Watkins, ..., W. F. DeGrado. 2022. Transient water wires mediate selective proton conduction in designed channel proteins. Preprint at bioRxiv. https://doi.org/10.1101/2022.03.28. 485852
- 60. Nagle, J. F., and H. J. Morowitz. 1978. Molecular mechanisms for proton transport in membranes. Proc. Natl. Acad. Sci. USA. 75:298-302.
- 61. Li, J., S. A. Shaikh, ..., E. Tajkhorshid. 2013. Transient formation of water-conducting states in membrane transporters. Proc. Natl. Acad. Sci. USA. 110:7696-7701.
- 62. Yue, Z., W. Chen, ..., J. Shen. 2017. Constant pH molecular dynamics reveals how proton release drives the conformational transition of a transmembrane efflux pump. J. Chem. Theory Comput. 13:6405–6414.
- 63. Pang, Y. T., Y. Miao, ..., J. A. McCammon. 2017. Gaussian accelerated molecular dynamics in NAMD. J. Chem. Theory Comput. 13:9-19.
- 64. Miao, Y., and J. A. McCammon, 2017. Gaussian accelerated molecular dynamics: theory, implementation, and applications. Annu. Rep. Comput. Chem. 13:231-278.
- 65. Eicher, T., H.-j. Cha, ..., K. M. Pos. 2012. Transport of drugs by the multidrug transporter AcrB involves an access and a deep binding pocket that are separated by a switch-loop. Proc. Natl. Acad. Sci. USA. 109:5687-5692.
- 66. Russell, R. B., and G. J. Barton. 1992. Multiple protein sequence alignment from tertiary structure comparison: assignment of global and residue confidence levels. Proteins. 14:309-323.
- 67. Roberts, E., J. Eargle, ..., Z. Luthey-Schulten. 2006. MultiSeq: unifying sequence and structure data for evolutionary analysis. BMC Bioinf. 7:382.
- 68. Robert, X., and P. Gouet. 2014. Deciphering key features in protein structures with the new ENDscript server. Nucleic Acids Res. 42:W320-W324.
- 69. Stevens, C. M., S. O. Babii, ..., H. I. Zgurskaya. 2022. Proton transfer activity of the reconstituted Mycobacterium tuberculosis MmpL3 is modulated by substrate mimics and inhibitors. Proc. Natl. Acad. Sci. USA. 119:e2113963119.
- 70. Takayama, K., C. Wang, and G. S. Besra. 2005. Pathway to synthesis and processing of mycolic acids in Mycobacterium tuberculosis. Clin. Microbiol. Rev. 18:81–101.